References

37. Jin KP, Sheng RF, Yang C, Zeng MS. Combined arterial and delayed enhancement patterns of MRI assist in prognostic prediction for intrahepatic mass-forming cholangiocarcinoma (IMCC). Abdom Radiol (NY) 2022;47:640-50.
38. Liao X, Zhang D. The 8th Edition American Joint Committee on Cancer Staging for Hepato-pancreato-biliary Cancer: A Review and Update. Arch Pathol Lab Med. 2021;145(5):543-553.
39. Aherne EA, Pak LM, Goldman DA, Gonen M, Jarnagin WR, Simpson AL, Do RK. Intrahepatic cholangiocarcinoma: can imaging phenotypes predict survival and tumor genetics? Abdom Radiol (NY) 2018;43:2665-72.
40. Renzulli M, Brocchi S, Cucchetti A, Mazzotti F, Mosconi C, Sportoletti C, Brandi G, Pinna AD, Golfieri R. Can Current Preoperative Imaging Be Used to Detect Microvascular Invasion of Hepatocellular Carcinoma? Radiology 2016;279:432-42.
41. Mulé S, Galletto Pregliasco A, Tenenhaus A, Kharrat R, Amaddeo G, Baranes L, Laurent A, Regnault H, Sommacale D, Djabbari M, Pigneur F, Tacher V, Kobeiter H, Calderaro J, Luciani A. Multiphase Liver MRI for Identifying the Macrotrabecular-Massive Subtype of Hepatocellular Carcinoma. Radiology 2020;295:562-71.
42. King MJ, Hectors S, Lee KM, Omidele O, Babb JS, Schwartz M, Tabrizian P, Taouli B, Lewis S. Outcomes assessment in intrahepatic cholangiocarcinoma using qualitative and quantitative imaging features. Cancer Imaging 2020;20:43.
43. Sheng R, Huang X, Jin K, Gao S, Zeng M, Wu D, Shi G. Contrast-enhanced MRI could predict response of systemic therapy in advanced intrahepatic cholangiocarcinoma. Eur Radiol 2022;32:5156-65.
44. Lee J, Kim SH, Kang TW, Song KD, Choi D, Jang KT. Mass-forming Intrahepatic Cholangiocarcinoma: Diffusion-weighted Imaging as a Preoperative Prognostic Marker. Radiology 2016;281:119-28.
45. Min JH, Kim YK, Choi SY, Kang TW, Lee SJ, Kim JM, Ahn S, Cho H. Intrahepatic Mass-forming Cholangiocarcinoma: Arterial Enhancement Patterns at MRI and Prognosis. Radiology 2019;290:691-9.
46. Yoh T, Cauchy F, Le Roy B, Seo S, Taura K, Hobeika C, Dokmak S, Farges O, Gelli M, Sa Cunha A, Adam R, Uemoto S, Soubrane O. Prognostic value of lymphadenectomy for long-term outcomes in node-negative intrahepatic cholangiocarcinoma: A multicenter study. Surgery 2019;166:975-82.

Table S1 MR imaging acquisition protocols

Parameter	T1-weighted IP and OP imaging	T2-weighted images (coronal)	T2-weighted imaging FS	Diffusion-weighted imaging	CE T1- weighted imaging	Late post-contrast (coronal)
Repetition time (ms)	3.6-4.5	957-10000	1440-7000	1248-4000	2.9-3.8	3.6-5.4
Echo time (ms)	1.2-2.9	68-94	76-100	46-76	1.1-1.6	1.0-2.6
Field of view (cm)	36-42	38-42	36-38	36-38	36-42	40-50
Acquisition matrix	288×224, 256×224, 320×193	320×288, 288×288, 320×224	320×224, 320×320, 320×220	140×140, 128×128, 128×83	256×192, 288×224, 288×151	352×256, 288×256, 288×185
Pixels (mm)	0.6-1.0	0.6-1.2	0.9-1.3	1.4-1.9	0.3-0.5	0.5-1.7
Temporal resolution (s/phase)	NA	NA	NA	NA	12-16.6	15-33
Section thickness (mm)	3.0-6.0	5.0-7.0	5.0-6.5	6.0-7.0	3.0-5.0	1.5-4.2
Gap (mm)	0.5-1.0	1.0	0.5-1.0	1.0-2.0	0	0
Flip angle (degree)	9-15	90, 145	150, 120	90	9-15	9-15

Data is the range of parameters on different magnetic resonance image machines. Except specifically mentioned, they are all scanned on the axial. MR, magnetic resonance; IP, in-phase; OP, opposed-phase; FS, fat-suppressed; CE, contrast-enhanced; NA, not applicable.

https://dx.doi.org/10.21037/qims-23-11

Table S2 MR imaging features: definition of imaging features and respective categories

Variables	Definitions	Categories
Tumor maximum diameter (37)	Tumor maximum diameter was measured the largest diameter on axial pre-contrast T1-weighted image. Based on the 8th edition of the American Joint Committee on Cancer (AJCC) staging system, the tumors were divided into two groups (38)	1, ≤5 cm; 2, >5 cm
Number of tumors (39)	Number of tumors was determined based on the number of tumor nodules in the liver, including satellite nodules and intrahepatic metastasis. Satellite nodules defined as tumors within 1 cm of the primary tumor border, and intrahepatic metastases defined as tumors >1 cm from the primary tumor	1, single; 2, multiple
Tumor margin (40)	Smooth: a clear demarcation of the entire tumor on the MRI images obtained in the delayed phase or transitional phase. Non-smooth: focal extranodular extension, multinodular confluent appearance, and focal infiltrative margin in the delayed phase	1, smooth; 2, infiltrative
Tumor necrosis (41)	Necrosis sign was a continuously unenhanced defect with high-signal intensity on T2-weighted fat-suppressed image and low signal on T1-weighted image	1, absent; 2, present
Bile duct dilatation	Evaluated on T2-weighted fat-suppressed or contrast enhanced images, including inner-tumor or peritumoural bile duct dilation	1, absent; 2, present
Hepatic capsule retraction (42)	unequivocal inward liver contour changes immediately superficial to an intrahepatic cholangiocarcinoma lesion	1, absent; 2, present
Peritumoral enhancement (43)	Fuzzy-marginated hyperenhancement outside the tumor borders on arterial-phase (AP) that becomes isointense with normal liver parenchyma in later dynamic phases	1, absent; 2, present
DWI signal characteristics (44)	Diffuse hypo-enhancement: less than one-third of the tumor showed diffusion restriction. Diffuse hyper-enhancement: more than one-third of the tumor showed diffusion restriction	1, diffuse hypo-enhancement; 2, diffuse hyper-enhancement
AP enhancement pattern (45)	Diffuse hypo-enhancement: the area of hyperenhancement was less than 10% of the tumor surface. Rim-enhancement: rim-enhancement, the area range of peripheral enhancement was 10%–70%. Diffuse hyper-enhancement: the area of hyper-enhanced was greater than 70% of the tumor surface	1, Diffuse hypo-enhancement; 2, rim-enhancement; 3, diffuse hyper-enhancement
Targetoid appearance (43)	Targetoid appearance including one of the following: rim arterial phase hyperenhancement, peripheral washout, delayed central enhancement, or targetoid restriction on diffusion-weighted imaging	1, absent; 2, present
Lymph node status (46)	When a lymph node presented 1 cm at least in short-axis diameter or a smaller lymph node with heterogeneous enhancement, round or irregular shape was considered as positive	1, positive; 2, negative

MR, magnetic resonance; DWI, diffusion-weighted images.

Table S3 Inter-observer agreements for each imaging feature

Variables	κ values (95% confidence intervals)
Number of tumors	0.888 (0.815, 0.961)
Tumor margin	0.761 (0.679, 0.843)
Necrosis	0.749 (0.657, 0.841)
Bile duct dilatation	0.874 (0.807, 0.941)
Capsule retraction	0.831 (0.757, 0.904)
Peritumoral enhancement	0.872 (0.805, 0.939)
DWI signal characteristics	0.767 (0.649, 0.885)
AP enhancement pattern	0.792 (0.712, 0.872)
Targetoid appearance	0.634 (0.516, 0.752)
Lymph node status	0.863 (0.794, 0.932)

Data are κ statistics with 95% confidence intervals in parentheses.

https://dx.doi.org/10.21037/qims-23-11

Table S4 Radiomics features' selection results

	Radiomic features	LASSO coefficient (β)
MVI status	Intercept	-0.09098416
	DWI_log.sigma.3.0.mm.3D_glrlm_LongRunLowGrayLevelEmphasis	0.22746793
	T2_log.sigma.5.0.mm.3D_glcm_ClusterShade	-0.08352660
	T2_log.sigma.2.0.mm.3D_glcm_Imc2	-0.01070164
	T2_wavelet.HHL_glszm_ZoneEntropy	0.14848064
	DWI_wavelet.HHH_glcm_SumEntropy	0.01244092
	T2_wavelet.LHH_firstorder_Kurtosis	0.08712179
	T2_wavelet.LLL_glszm_SmallAreaLowGrayLevelEmphasis	-0.16539808
	T2_log.sigma.5.0.mm.3D_firstorder_Skewness	-0.11850991
	DWI_original_shape_Flatness	-0.01091418
	T2_wavelet.HHL_gldm_DependenceVariance	0.12000406
	DWI_wavelet.HLL_glszm_SmallAreaHighGrayLevelEmphasis	0.14940092
	T2_wavelet.HHH_firstorder_Median	-0.09095953
	T2_wavelet.LHL_gldm_DependenceEntropy	0.03645931
	T2_wavelet.LLL_glcm_Imc2	-0.17710026
	DWI_wavelet.HHL_gldm_DependenceNonUniformityNormalized	-0.21121682
	T2_wavelet.LHH_glszm_ZoneEntropy	0.02886081
Tumor grading	Intercept	0.4957142100
	T2_wavelet.LHH_glcm_JointEnergy	-0.1130100795
	T2_wavelet.HLL_glcm_Imc1	0.0099504462
	DWI_wavelet.LLL_gldm_LargeDependenceHighGrayLevelEmphasis	0.0403740211
	T2_wavelet.LLH_glcm_Imc2	-0.0007046255
	T2_log.sigma.2.0.mm.3D_firstorder_Kurtosis	0.0731579396
	T2_wavelet.HLH_glcm_Imc1	0.1669030819
	DWI_log.sigma.2.0.mm.3D_glcm_Imc2	-0.0562923291
	DWI_original_shape_Elongation	0.2322154964
	T2_wavelet.HHH_gldm_DependenceVariance	-0.0848792990

The intraclass correlation coefficient of selected features all >0.8. MVI, microvascular invasion; DWI, diffusion-weighted images; LASSO, least absolute shrinkage and selection operator; glcm, gray-level co-occurrence matrix; glszm, gray-level size zone matrix; glrlm, gray-level run-length matrix; gldm, gray-level dependence matrix; log, Laplacian of Gaussian; H, high-pass filter; L, low-pass filter.

Table S5 Comparison of different models by the Delong test

	Group	Model	Radiomics model	Nomogram model
MVI	Training set	Clinical model	0.326	<0.001
		Radiomics model	-	0.009
	Validation set	Clinical model	0.596	0.008
		Radiomics model		0.055
Tumor grading	Training set	Clinical model	0.003	<0.001
		Radiomics model	-	0.313
	Validation set	Clinical model	0.544	0.002
		Radiomics model	-	0.095

P values <0.05 was defined as statistical significance. MVI, microvascular invasion.

https://dx.doi.org/10.21037/qims-23-11

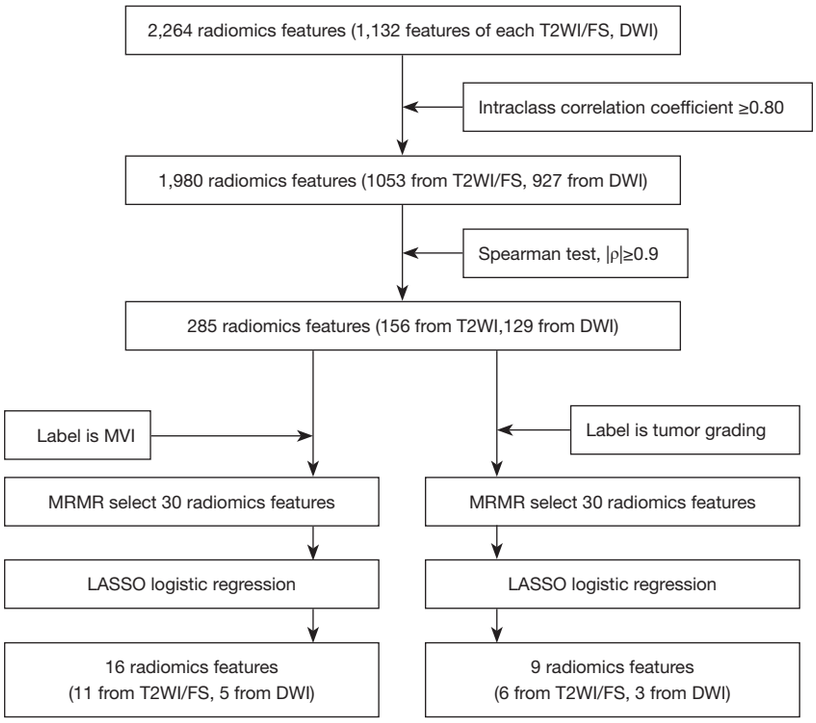

Figure S1 Radiomics features selection pipeline. T2WI/FS, T2 weighted imaging/fat-suppressed; DWI, diffusion weighted imaging; MVI, microvascular invasion; MRMR, minimum redundancy maximum relevance; LASSO, least absolute shrinkage and selection operator.

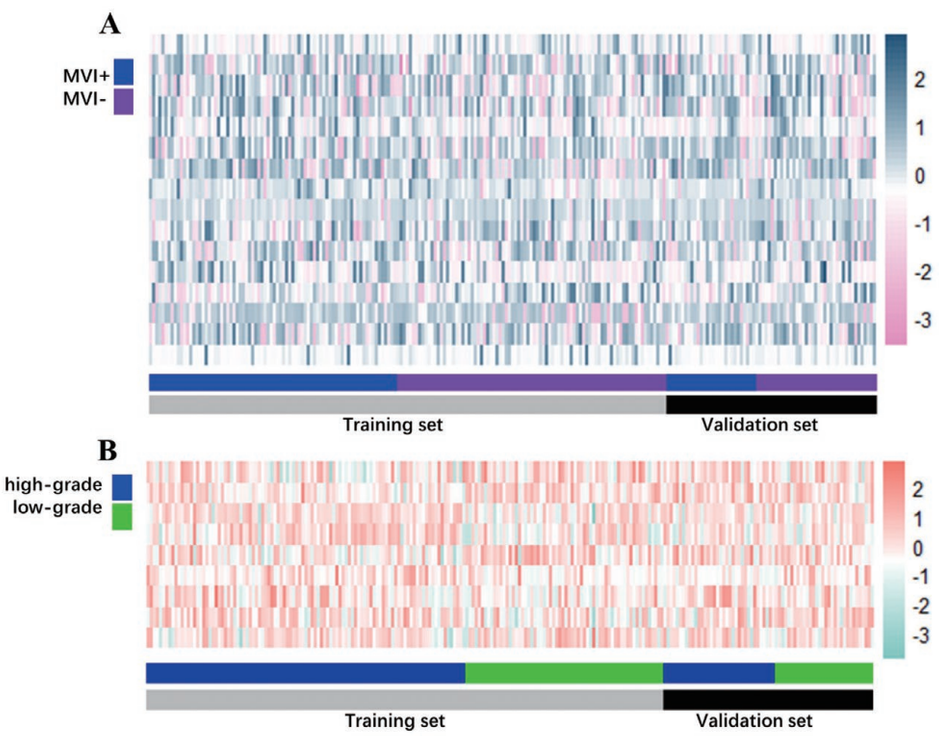

Figure S2 Heatmap of the significant radiomics features. Each column corresponds to one patient, and each row corresponds to the Z-scores of the normalized radiomics features. The heatmap is grouped for the training and validation sets for prediction of MVI (A) and tumor grading (B). Sixteen radiomics features were selected for MVI and 9 radiomics features were selected for tumor grading. MVI, microvascular invasion.

https://dx.doi.org/10.21037/qims-23-11

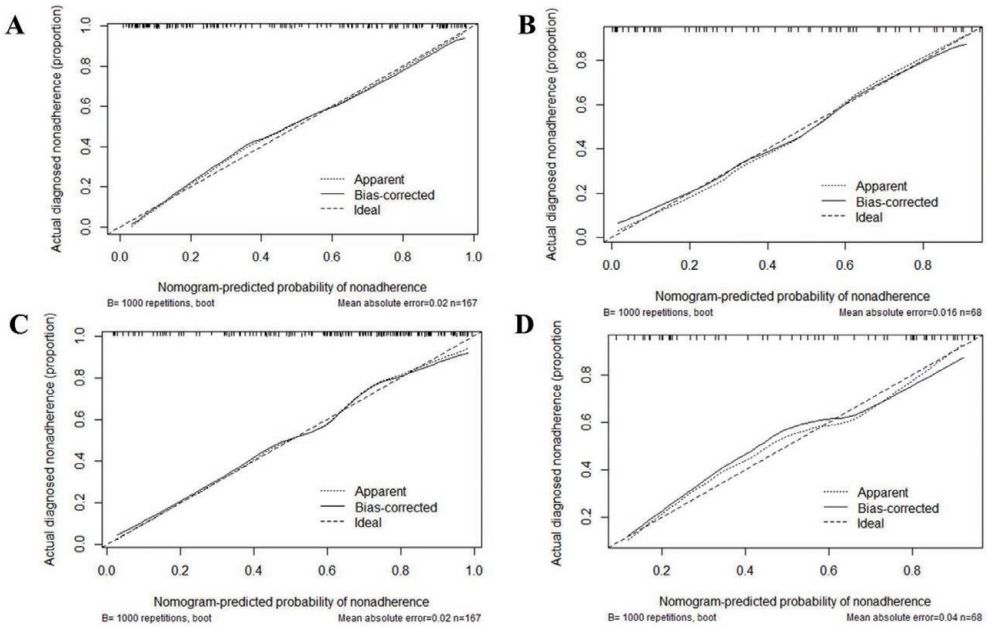

Figure S3 Calibration curve of the nomogram in training set for the prediction of MVI (A) and tumor high-grading (C). Calibration curve of the nomogram in validation set for the prediction of MVI (B) and tumor high-grading (D). The 45° dotted line represents a perfect prediction. The solid line represents the predictive performance of the nomogram. The solid line has a close fit to the dotted gray line, which indicates good predictive capability of the nomogram. Hosmer-Lemeshow test showed good calibration in the training (P=0.895) (A) and validation (P=0.762) (B) sets in the prediction of MVI. P values were 0.451 (C) and 0.254 (D) based on the Hosmer-Lemeshow test in the training and validation sets in the prediction of tumor grading. MVI, microvascular invasion.

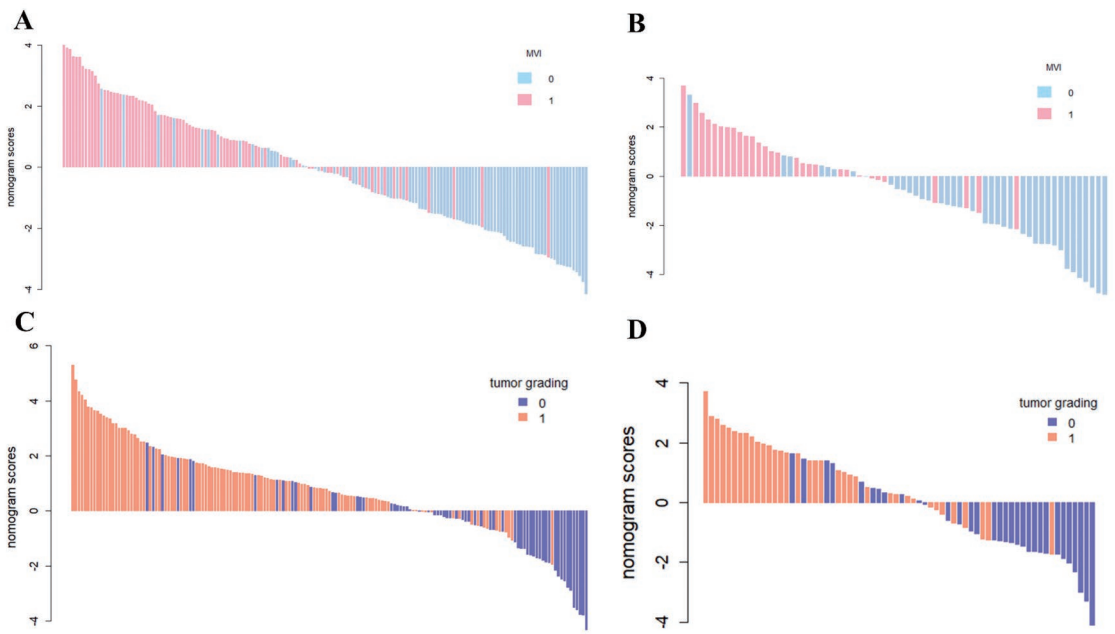

Figure S4 The radiomic nomogram scores for each patient in the training (A) and validation (B) sets for the prediction of MVI. The radiomic nomogram scores for each patient in the training (C) and validation (B) sets for the prediction of tumor grading. MVI, microvascular invasion.

https://dx.doi.org/10.21037/qims-23-11

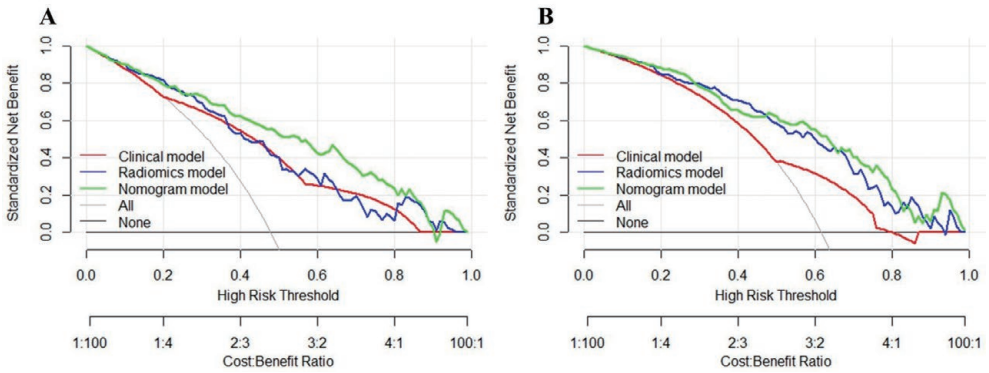

Figure S5 DCA for the radiomics nomogram in the training set. The x-axis represents the threshold probability, and the y-axis represents the net benefit. The "All" line represents the hypothesis that all patients had MVI (A) or high-grading (B). The "None" line indicates the hypothesis that no patients were MVI (A) or high-grading (B). The red (using clinical characteristics), blue (using radiomics signature), and green (using nomogram) lines represent the net benefits of different diagnostic models at given threshold probability for the prediction of MVI+ (A) and high-grading (B). DCA, decision curve analysis; MVI, microvascular invasion.

https://dx.doi.org/10.21037/qims-23-11